Electronic and magnetic properties of the Jahn-Teller active fluoride $NaCrF_3$ from first-principles calculations

Jianghan Bao,[1,2] Di Wang,[1,2,*] Hai-Zhou Lu,[3] and Xiangang Wan[1,2]

[1]*National Laboratory of Solid State Microstructures and School of Physics, Nanjing University, Nanjing 210093, China*

[2]*Collaborative Innovation Center of Advanced Microstructures, Nanjing University, Nanjing 210093, China*

[3]*Shenzhen Institute for Quantum Science and Engineering and Department of Physics, Southern University of Science and Technology, Shenzhen 518055, China*

(Received 20 May 2020; revised 7 November 2020; accepted 7 December 2020; published 24 December 2020)

In perovskite-type compounds, the interplay of the cooperative Jahn-Teller effect, electronic correlations, and orbital degrees of freedom leads to intriguing properties. $NaCrF_3$ is a newly synthesized Jahn-Teller active fluoroperovskite where the CrF_6^{4-} octahedrons are considerably distorted. Based on the first-principles calculation, we analyze its electronic structure and magnetic properties. Our numerical results show that the Cr^{2+} ions adopt the high-spin $t_{2g\uparrow}^3 e_{g\uparrow}^1$ configuration and the material exhibits *G*-type orbital ordering. We also estimate the magnetic exchange couplings and find that the in-plane and interplanar nearest-neighbor interactions are ferromagnetic and antiferromagnetic, respectively. The ground state of this material is *A*-type antiferromagnetic, in agreement with the experiments. Our results give a complete explanation of its electronic structure and magnetic and orbital order, and help to further comprehend the behaviors of Jahn-Teller active perovskite-type fluoride.

DOI: 10.1103/PhysRevB.102.245142

I. INTRODUCTION

In strongly correlated electron systems, the interplay between charge, spin, orbital, and lattice degrees of freedom gives rise to profuse and exotic physics properties [1]. In particular, the orbital physics is usually significant and inevitable for understanding this complexity [2,3]. A fascinating example is the cooperative Jahn-Teller (JT) effect, which refers to a symmetry-lowering structural deformation driven by the coupling between the degenerate orbital states and the collective lattice vibrations [4–8]. Accompanied with strong electronic correlations and orbital degrees of freedom, the cooperative JT effect gives rise to intriguing behaviors in perovskite-type compounds [6,9]. The best known example is the parent material of colossal magnetoresistance (CMR) manganites, $LaMnO_3$ [10,11], where the cooperative JT effect plays a fundamental role in stabilizing the *A*-type antiferromagnetic (AFM) spin and *C*-type orbital ordering (OO) [12–15]. Moreover, it arouses the formation of polarons, which is regarded as a key mechanism in the CMR effect [16–18].

Besides in the perovskite oxides, the cooperative JT effect also causes various remarkable magnetic and structural effects in fluoroperovskites [19–35]. In the paradigmatic example, tetragonal $KCuF_3$, two distinct types of collective JT distortions lead to two isoenergetic structural polytypes [19–22]. The cooperative JT effect is not only essential for stabilizing the antiferro-orbital order in $KCuF_3$ at high temperature [23], but also makes this compound one of the most ideal one-dimensional antiferromagnets with $S = \frac{1}{2}$ [9,19]. Similar uniform AFM chains induced by the cooperative JT effect are also found in triclinic $AgCuF_3$ and $NaCuF_3$ [26,27]. Additionally, chromium fluoroperovskites are also able to activate the cooperative JT effect, such as $KCrF_3$ [28–30]. This material has rich structural phase transitions ($Pm3m \rightarrow I4/mcm$ at 973 K and $I4/mcm \rightarrow I112/m$ at 250 K) [28–30] and exhibits an ordering of staggered $3d_{3x^2-r^2}$ and $3d_{3y^2-r^2}$ orbitals in the *ab* plane which is rotated by 90° in consecutive layers along the *c* direction at room temperature [28,29]. The magnetic ground state of $KCrF_3$ is an *A*-type antiferromagnetic spin-ordered structure with Néel temperature 79.5 K [30]. In recent years, the ample structural and magnetic behaviors of $KCrF_3$ have attracted much interest in theoretical study [31–35].

Recently, another chromium fluoroperovskite, $NaCrF_3$, was successfully synthesized with a novel wet chemistry method [36]. Incorporating the JT active Cr ions, this material exhibits obvious cooperative structural distortions. Neutron powder diffraction experiments revealed that $NaCrF_3$ adopts a canted *A*-type AFM ground state at low temperature [36]. The Curie-Weiss temperature and Néel temperature were given as −4 and 21.3 K, respectively [36]. Its Néel temperature is much lower than that of $KCrF_3$ (79.5 K) [30], indicating its weak antiferromagnet nature. Isostructural with triclinic $NaCuF_3$ [26,36], $NaCrF_3$ has considerably lower crystal symmetry than $KCrF_3$. Meanwhile, the Cr ions of $NaCrF_3$ have $3d^4$ electronic configuration, which are different from the $3d^9$ Cu ions in $KCuF_3$. Thus, it will be worthwhile to investigate the electronic structure and magnetic properties of this distinct compound.

In this paper we systematically analyze the electronic and magnetic properties of $NaCrF_3$ by using the first-principles calculation. Band structure and partial density of states (PDOS) show clearly the splitting of e_g orbitals of Cr^{2+} ions caused by the axial elongation of CrF_6^{4-} octahedrons.

*Corresponding author: diwang0214@nju.edu.cn

Our numerical results show that this material exhibits *G*-type antiferro-orbital ordering while the Cr^{2+} ions adopt the high-spin $t_{2g\uparrow}^3 e_{g\uparrow}^1$ configuration. An *A*-type AFM spin state is found to own the lowest total energy in accordance with the experiments. Based on an energy-mapping procedure, a ferromagnetic (FM) in-plane nearest-neighbor (NN) coupling, an AFM interplanar NN interaction and non-negligible interplanar next-nearest-neighbor (NNN) exchange parameters are estimated. Through mean-field approximation theory, we calculate the Néel temperature, which is in reasonable agreement with the result of the experiment. The ground magnetic state of *A*-type magnetic order can be understood based on the electronic configuration of Cr^{2+} ions and the Cr-F-Cr superexchange pathways.

II. METHOD AND CRYSTAL STRUCTURE

The density functional calculations have been performed by utilizing the full potential linearized augmented plane-wave (LAPW) method as implemented in the WIEN2K code [37]. The local spin density approximation (LSDA) is adopted as the exchange-correlation potential [38]. To take into account the Coulomb repulsion of the Cr 3*d* electrons, the LSDA + *U* scheme is also performed [39]. The value of U_{eff} ($U_{\text{eff}} = U - J$, where the Hund exchange parameter *J* is set to be zero), which varies from 4 to 8 eV, has been widely used in previous first-principles calculation [20,31]. We found that our numerical essential properties, which refer to the qualitative features such as occupancy of *d* electrons, orbital ordering, and magnetic ground state, do not depend on the value of U_{eff} in this range and the results of $U_{\text{eff}} = 6$ eV are mainly presented here. The muffin-tin sphere radii are chosen to be 2.06, 1.81, and 1.90 bohrs for Na, F, and Cr atoms, respectively. The plane-wave cutoff $K_{\max}$ is determined by $R_{\min}K_{\max} = 7$, where the $R_{\min}$ is the smallest of all atomic sphere radii; thus the $K_{\max}$ is given by 3.87 approximately. The number of plane waves at the Γ point is 1667. The convergence criterion of the crystal total energy is set to be 0.01 mRy per conventional unit cell, and a $17\times16\times11$ *k* mesh is used for the integration over the Brillouin zone, which both ensure the numerical accuracy of the calculation. In addition to the FM configuration, five possible AFM configurations (shown in Fig. 4) have also been taken into consideration to explore the magnetic properties of $NaCrF_3$. Additionally, two of these AFM configurations (AFM-1 and AFM-3 in Fig. 4) need a $\sqrt{2}\times\sqrt{2}\times1$ supercell and a $12\times11\times11$ *k* mesh.

The experimental crystal structure [Fig. 1(a)] obtained by high-resolution synchrotron x-ray and neutron powder diffraction is used in the calculation [36]. $NaCrF_3$ belongs to the triclinic crystal system (space group $P\bar{1}$), with lattice constants $a = 5.48428(11)$ Å, $b = 5.67072(11)$ Å, and $c = 8.13620(15)$ Å. The angles between the lattice vectors are $\alpha = 90.3860(10)^\circ$, $\beta = 90.2816(8)^\circ$, and $\gamma = 86.3255(8)^\circ$ [36]. A minimization of internal parameters is performed and the criterion of the remaining force is set to be 0.5 mRy/bohr. Four inequivalent crystallographic sites are occupied by the Cr cations [Fig. 1(a)], which form distorted corner-sharing CrF_6 octahedrons enclosed in a Na cage with the surrounding F anions. Each axially elongated CrF_6 octahedra has two long and four short Cr-F bonds. It should also be noted that the

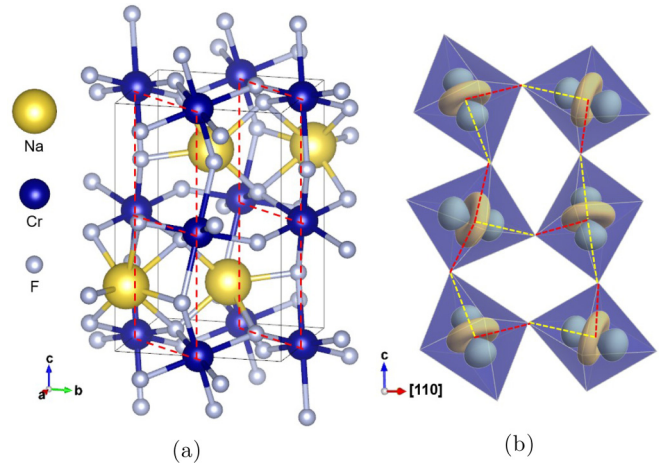

FIG. 1. (a) Crystal structure of $NaCrF_3$ [36]. Na, Cr, and F atoms are represented here by yellow, blue, and grey spheres, respectively. Red dashed lines indicate the $(1\bar{1}0)$ plane. (b) Schematic view of occupied $d_{3z^2-r^2}$ orbitals of Cr^{2+} and corresponding distorted CrF_6^{4-} octahedrons in $(1\bar{1}0)$ plane; yellow and red dashed lines denote the alternating long and short Cr-F bonds. Notice that the lobes of $d_{3z^2-r^2}$ point in the direction of long Cr-F bonds.

CrF_6 octahedrons connect with each other through alternating long-short Cr-F bonds within the $(1\bar{1}0)$ plane, while all the interplanar connections consist of short bonds [Fig. 1(b)].

III. RESULTS AND DISCUSSION

The local density approximation (LDA) calculation is carried out first to clarify the basic electronic features. The band structures and the density of states (DOS) are given in Figs. 2(a) and 3(a). The *z* direction of the local coordinate system is defined along the longest Cr-F bond of each CrF_6 octahedron in the analysis of PDOS. There are 12 F ions in the conventional unit cell. As shown in Figs. 2(a) and 3(a), 36 F 2*p* bands mainly locate in the energy range from −9 to −6 eV, indicating that the F 2*p* orbitals are nearly fully occupied. In comparison, the F 2*p* bands of $KCuF_3$, which locates between −7 and −3 eV, are closer to the Fermi level due to the stronger electronegativity of Cu than Cr. As shown in Fig. 3(a), the main contribution of Na bands is above the Fermi level, while there is also a small distribution of Na states between −9 and −6 eV, indicating the non-negligible hybridization between Na and F states. Thus the nominal chemical valence of F and Na can be regarded as −1 and +1, respectively. As a consequence, the nominal valence of Cr is +2 and the outer-shell electronic configuration of the Cr ion is $3d^4$. Our results also show that the bands around the Fermi level consist mostly of the Cr 3*d* electrons [Fig. 3(a)]. In each axially elongated CrF_6 octahedron, two long Cr-F bonds are collinear, while the angles between the long bonds and the short bonds deviate slightly from the right angle (ranging from 84.50° to 96.17°) [36]. Although the CrF_6 octahedrons deform from the ideal ones, the Cr 3*d* orbitals can still be divided into 12 t_{2g} bands (from −0.47 to 0.25 eV) and 8 e_g bands (from 0.45 to 2.30 eV), as shown in Figs. 2(a) and 3(a). Furthermore, influenced by the axial elongation of the CrF_6

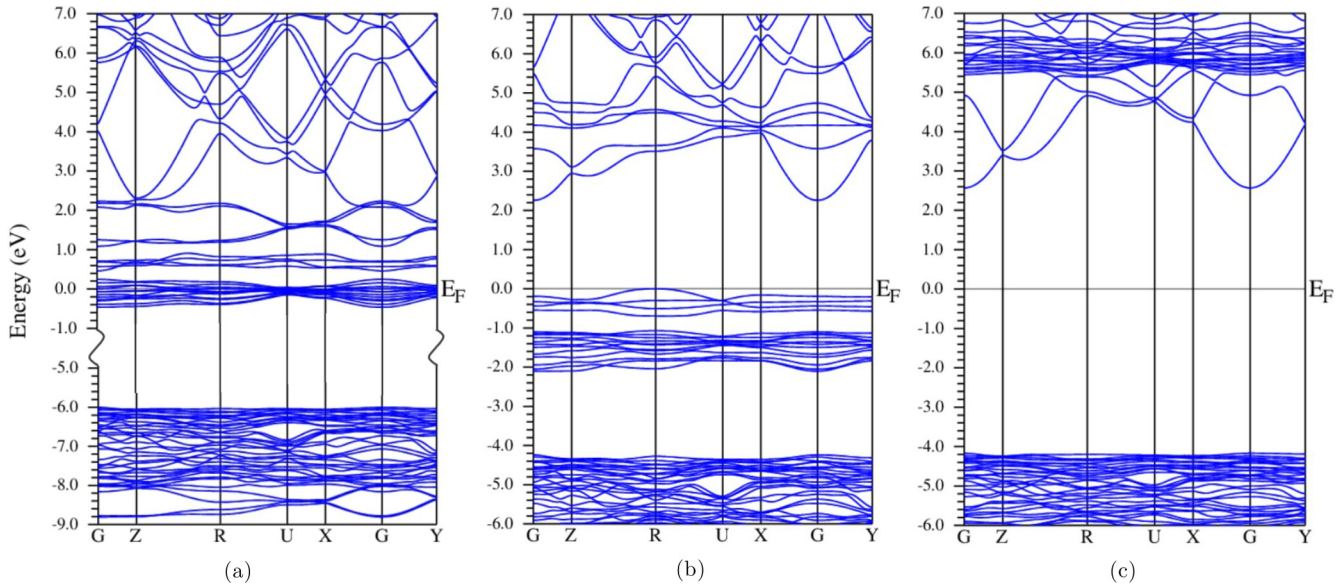

FIG. 2. Electronic structure of $NaCrF_3$. (a) The results of LDA calculation. No band occurs in the omitted part (from −5 to −1 eV). (b) The spin-up channel. (c) The spin-down channel given by LSDA + U ($U = 6$ eV) calculation with FM configuration. The Fermi level is set to be zero.

octahedrons, the e_g states split into four $d_{3z^2-r^2}$ bands from 0.45 to 0.92 eV and four $d_{x^2-y^2}$ bands from 1.08 to 2.30 eV, as shown in Figs. 2(a) and 3(a). The energy splitting between the band centers of $d_{3z^2-r^2}$ and $d_{x^2-y^2}$ states is estimated to be about 1.01 eV.

As shown in Fig. 3(a), the DOS at the Fermi level is quite large, which indicates the electronic instability. To explore its magnetic properties, the LSDA + U calculation of the FM configuration is performed. For $U = 6$ eV, the band structures are shown in Figs. 2(b) and 2(c). The spin exchange splitting is relatively large and the down-spin bands lie far away from the Fermi level. As shown in the band structure and DOS [Figs. 2(b), 2(c), and 3(c)], the t_{2g} and $d_{3z^2-r^2}$ orbitals in the spin-up channel are fully occupied, while the $d_{x^2-y^2}$ orbitals are entirely empty in the FM structure. Thus, the Cr $3d^4$ configuration can be regarded as holding a $t^3_{2g\uparrow} e^1_{g\uparrow}$ high-spin state. An occupied $d_{3z^2-r^2}$ orbital points to the direction of the longest Cr-F bond of each octahedron, which is different from all its nearest neighbors. Thus, we deduce that the occupied $d_{3z^2-r^2}$ orbitals form a G-type orbital ordering pattern, as shown in Fig. 1(b). Enhanced by the combination of the JT effect and electronic correlation, the energy splitting between the weight centers of $d_{x^2-y^2}$ and $d_{3z^2-r^2}$ states in the spin-up channel is estimated to be 4.5 eV. This value is larger than that of $U = 4$ eV and smaller than that of $U = 8$ eV, which are approximately given by 2.8 and 5.3 eV [Figs. 3(b) and 3(d)], respectively. The high-spin-state Cr^{2+} ions and G-type orbital order show remarkable similarity with those of $KCrF_3$ [31–33,35].

In order to study the magnetic ground state of $NaCrF_3$, five AFM configurations have been taken into consideration in addition to the FM state (see Fig. 4 for the schematic descriptions of the different AFM configurations). AFM-1 and AFM-2 are two different A-type AFM structures where the AFM couplings are in the $[1\bar{1}0]$ and [001] directions, respectively. Opposite to AFM-1, the Cr^{2+} ions of the AFM-3 configuration (C type) couple antiferromagnetically in the $(1\bar{1}0)$ plane, but ferromagnetically in the $[1\bar{1}0]$ direction. And in AFM-4 (C type), the magnetic moments are antiparallel in the ab plane, but parallel in the c direction. In the spin configuration AFM-5 (G type), each spin is set to be antiparallel to all its nearest neighbors.

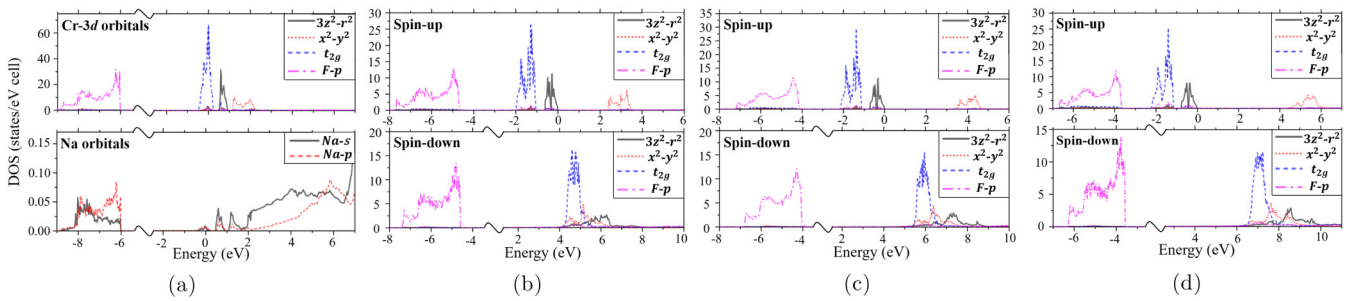

FIG. 3. Partial density of states (PDOS) of $NaCrF_3$ given by different types of calculations: (a) LDA, (b) LSDA + U ($U = 4$ eV), (c) LSDA + U ($U = 6$ eV), and (d) LSDA + U ($U = 8$ eV). The local coordinate system is used with the z direction defined along the longest Cr-F bond of each CrF_6 octahedron in the calculation of PDOS.

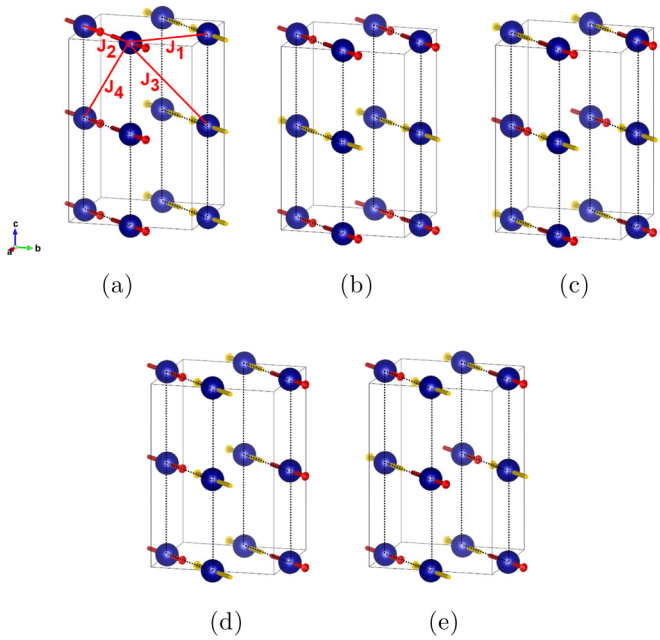

FIG. 4. Five AFM configurations considered in our density functional theory (DFT) calculations: (a) AFM-1, (b) AFM-2, (c) AFM-3, (d) AFM-4, and (e) AFM-5 spin structures, respectively. AFM-1 and AFM-2 are *A*-type AFM where the AFM couplings are in the $[1\bar{1}0]$ and [001] directions, respectively. AFM-3 and AFM-4 are *C*-type AFM where the FM couplings are in the $[1\bar{1}0]$ and [001] directions, respectively. AFM-5 is a *G*-type configuration. Blue spheres stand for the Cr atoms within the $(1\bar{1}0)$ plane which is represented by the dashed lines. Red arrows denote spins in the up direction and yellow arrows denote spins in down direction. The four exchange parameters that we take into consideration are shown in (a).

Our numerical results reveal that different magnetic configurations have minor influence on the electronic configuration and the orbital ordering of the material. Every spin configuration has the same pattern of a high-spin $t^3_{2g\uparrow}e^1_{g\uparrow}$ state and the *G*-type orbital order. The differences between total energies for the LSDA + *U* calculations are summarized in Table I. The magnetic moments of Cr^{2+} of various magnetically ordered structures are also listed in this table. The results show that the AFM-1 configuration has the lowest total energies under different *U* values, which is in agreement with the experimental results [36]. The calculated magnetic moments of different spin configurations are similar, which

TABLE I. Relative total energies ($E_{\rm tot}$ in meV/f.u.) of different magnetic ordering states and corresponding magnetic moment (M_{Cr} in μ_B) of Cr^{2+} obtained by LSDA + *U* calculations, total energy of AFM-1 structure is set to be 0.

	U (eV)	FM	AFM-1	AFM-2	AFM-3	AFM-4	AFM-5
$E_{\rm tot}$	4	2.74	0	5.50	8.98	5.67	8.73
	6	2.02	0	3.46	5.27	3.57	4.86
	8	1.74	0	2.58	3.49	1.91	3.02
M_{Cr}	4	3.380	3.374	3.375	3.369	3.368	3.364
	6	3.432	3.429	3.429	3.425	3.425	3.422
	8	3.449	3.447	3.447	3.444	3.444	3.442

TABLE II. Calculated exchange constants (meV) for different computational settings. Néel temperatures (K) given by mean-field approximation with different *U* values.

U (eV)	J_1	J_2	J_3	J_4	Néel
4	0.130	−0.477	0.044	−0.034	61.61
6	0.107	−0.261	0.029	−0.034	37.66
8	0.123	−0.151	0.021	−0.013	24.87

indicates that the magnetism of $NaCrF_3$ is quite localized and the total energy differences mainly originate from the interatomic exchange interactions. Thus, it allows us to perform the energy-mapping procedure to estimate the exchange couplings.

The exchange couplings are analyzed by using the Heisenberg Hamiltonian

$$H = \sum_{i<j} J_{ij}\mathbf{S}_i \cdot \mathbf{S}_j, \tag{1}$$

where J_{ij} stands for the spin exchange parameter between two spins at sites *i* and *j*. We have calculated the exchange parameters J_{ij} by using the relative total energies of different magnetic ordering systems. The exchange interactions that we consider are shown in Fig. 4(a), where J_1 and J_3 denote the NN and NNN interactions between the $(1\bar{1}0)$ planes, while J_2 and J_4 represent the NN and NNN couplings within the $(1\bar{1}0)$ planes.

By applying the spin Hamiltonian model [Eq. (1)] on the six different magnetic configurations, the total energies per conventional unit cell are expressed as follows:

$$\begin{aligned}
E_{FM} &= E_0 + 4(J_1 + 2J_2 + 4J_3 + 2J_4)S^2,\\
E_{AFM1} &= E_0 + 4(-J_1 + 2J_2 - 4J_3 + 2J_4)S^2,\\
E_{AFM2} &= E_0 + 4(J_1 - 2J_4)S^2,\\
E_{AFM3} &= E_0 + 4(J_1 - 2J_2 - 4J_3 + 2J_4)S^2,\\
E_{AFM4} &= E_0 + 4(-J_1 - 2J_4)S^2,\\
E_{AFM5} &= E_0 + 4(-J_1 - 2J_2 + 4J_3 + 2J_4)S^2.
\end{aligned}$$

Here E_0 denotes the paramagnetic part of the total energy, which is considered irrelevant of the change of spin configuration. The values of the exchange parameters *J* can be evaluated by mapping these energies obtained with LSDA + *U* calculations. Since the number of magnetic configurations is larger than the number of exchange parameters, a least-squares method is applied.

The calculated exchange couplings from the energy-mapping analysis are given in Table II. Generally speaking, the magnetic exchanges are considerably weaker in $NaCrF_3$ than in other materials with similar Jahn-Teller active ions [26,31,32,35]. With the value of *U* increasing, the values of most magnetic couplings decrease as expected. The dominant terms are J_1 and J_2, where the positive J_1 indicates an interplanar AFM interaction, while the negative J_2 reveals a FM coupling within the $(1\bar{1}0)$ plane. The results correspond well with experiments, since the combination of these NN interactions leads to the *A*-type magnetic ground state. When the value of *U* is set to be 6 eV, the prominent *J* in $NaCrF_3$

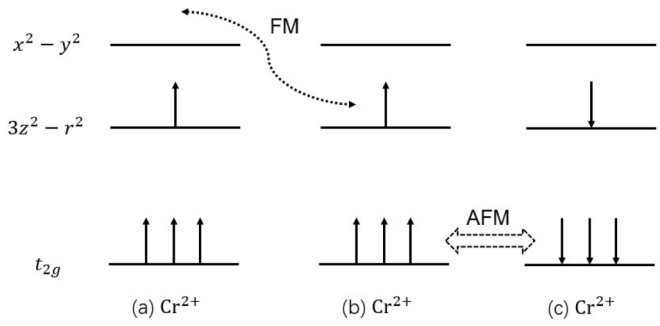

FIG. 5. Diagram of crystal levels of high-spin Cr^{2+} of different Cr^{2+} sites. The notations of the orbitals are given based on the local coordinate system of each Cr^{2+}. (a), (b) Two NN Cr^{2+} within the $(1\bar{1}0)$ plane, and (c) the NN Cr^{2+} of (b) in another plane. The in-plane e_g electron hopping leads to FM interaction while the interplanar coupling between t_{2g} orbitals results in AFM interaction.

is much smaller than the one in $KCrF_3$ [31]. As shown in Table II, J_1 and J_2 have the same order of magnitude, indicating that $NaCrF_3$ exhibits a three-dimensional magnetic nature. Moreover, we find that the interplanar NNN exchange constants J_3 and J_4 are non-negligible.

According to the experiments [36], the Curie-Weiss temperature θ in $NaCrF_3$ is -4 K while the Néel temperature T_N in $NaCrF_3$ is 21.3 K, smaller than that of $KCrF_3$ ($T_N = 79.5$ K) [30]. The relative low value of the frustration index $\frac{|\theta|}{T_N}$ (smaller than 1) reveals the interplay of the FM and AFM interactions [40]. Our calculated results of spin exchange couplings also verify the coexistence of the FM and AFM interactions. Based on the spin exchange parameters, we calculate the Néel temperature with different U values by the mean-field approximation theory [41], as shown in Table II. Since the mean-field approximation theory often overestimates the Néel temperature, we regard 6 eV as a reasonable choice among these U values.

It should be noted that the ground state with A-type AFM structure can be understood based on the superexchange pathways and electronic occupation (Fig. 3) in orbital order. Schematic crystal field levels and two possible exchange pathways are presented in Fig. 5. Two NN Cr^{2+} ions within the $(1\bar{1}0)$ plane are given by Figs. 5(a) and 5(b), while Fig. 5(c) represents the interplanar NN Cr^{2+} ion of Fig. 5(b). Note that the local $d_{3z^2-r^2}$ states point to the direction of the longest Cr-F bond while the pathways in the $(1\bar{1}0)$ plane connect through alternating long-short Cr-F bonds as shown in Fig. 1(b); therefore, the hopping between these $d_{3z^2-r^2}$ orbitals would be small. Within the $(1\bar{1}0)$ plane, the in-plane superexchange couplings are mainly via the hopping between the $d_{3z^2-r^2}$ and $d_{x^2-y^2}$ orbitals. According to the second Goodenough-Kanamori-Anderson (GKA) rule [42–45], a FM interaction within the $(1\bar{1}0)$ plane emerges through the virtual hopping of the half-filled $d_{3z^2-r^2}$ state and the empty $d_{x^2-y^2}$ state. As for the interplanar magnetic interaction, since the $d_{3z^2-r^2}$ states are lying in the $(1\bar{1}0)$ plane and the $d_{x^2-y^2}$ states are unoccupied, the interplanar hopping between e_g states is small. Thus the interplanar exchange is mainly via the virtual hopping between t_{2g} orbitals. By applying the first GKA rule [42–45], we have that the interplanar exchange between the half-filled t_{2g} states is AFM, since the hopping between half-filled states with same spin orientation is forbidden by the Pauli exclusion principle. These together make the magnetic ground state of $NaCrF_3$ to be the AFM-1 magnetic configuration.

IV. CONCLUSION

In conclusion, we have presented a comprehensive investigation of the newly synthesized JT active ternary fluoroperovskite $NaCrF_3$ through the DFT calculation. The high-spin configuration of Cr^{2+} and the G-type orbital ordering are proposed by our numerical results. We also confirmed the A-type AFM magnetic ground state obtained by the experiments. With the energy-mapping procedure, we estimate the exchange parameters. The interplanar NN interaction J_1 is AFM while in-plane NN coupling J_2 is FM. Based on the electronic occupation of Cr^{2+} ions in orbital order and the superexchange pathways, the magnetic ground state of A-type AFM order is understood. We hope our calculation of this compound may help to further understand of the behaviors in JT active perovskite fluoride.

ACKNOWLEDGMENTS

This work is supported by the National Natural Science Foundation of China (NSFC) (Grants No. 12004170, No. 11834006, No. 11525417, No. 51721001, and No. 11790311), the National Key R&D Program of China (Grants No. 2018YFA0305704 and No. 2017YFA0303203) and Natural Science Foundation of Jiangsu Province, China (Grant No. BK20200326). H.-Z.L. is supported by the NSFC (Grant No. 11925402). X.W. also acknowledges the support from the Tencent Foundation through the XPLORER PRIZE.

[1] M. Imada, A. Fujimori, and Y. Tokura, Metal-insulator transitions, Rev. Mod. Phys. **70**, 1039 (1998).

[2] Y. Tokura and N. Nagaosa, Orbital physics in transition-metal oxides, Science **288**, 462 (2000).

[3] G. Khaliullin, Orbital order and fluctuations in Mott insulators, Prog. Theor. Phys. Supp. **160**, 155 (2005).

[4] H. A. Jahn and E. Teller, Stability of polyatomic molecules in degenerate electronic states. I. Orbital degeneracy, Proc. R. Soc. London A **161**, 220 (1937).

[5] G. A. Gehring and K. A. Gehring, Co-operative Jahn-Teller effects, Rep. Prog. Phys. **38**, 1 (1975).

[6] K. I. Kugel and D. I. Khomskii, The Jahn-Teller effect and magnetism: Transition metal compounds, Phys. Usp. **25**, 231 (1982).

[7] D. I. Khomskii and K. I. Kugel, Elastic interactions and superstructures in manganites and other Jahn-Teller systems, Phys. Rev. B **67**, 134401 (2003).

[8] I. Bersuker, *The Jahn-Teller Effect* (Cambridge University Press, Cambridge, UK, 2006).

[9] D. I. Khomskii, *Transition Metal Compounds* (Cambridge University Press, Cambridge, UK, 2014).

[10] S. Jin, T. H. Tiefel, M. McCormack, R. A. Fastnacht, R. Ramesh, and L. H. Chen, Thousandfold change in resistivity in magnetoresistive La-Ca-Mn-O films, Science **264**, 413 (1994).

[11] M. B. Salamon and M. Jaime, The physics of manganites: Structure and transport, Rev. Mod. Phys. **73**, 583 (2001).

[12] D. D. Sarma, N. Shanthi, S. R. Barman, N. Hamada, H. Sawada, and K. Terakura, Band Theory for Ground-State Properties and Excitation Spectra of Perovskite LaMO$_3$ (M = Mn, Fe, Co, Ni), Phys. Rev. Lett. **75**, 1126 (1995).

[13] I. Solovyev, N. Hamada, and K. Terakura, Crucial Role of the Lattice Distortion in the Magnetism of LaMnO$_3$, Phys. Rev. Lett. **76**, 4825 (1996).

[14] E. Pavarini and E. Koch, Origin of Jahn-Teller Distortion and Orbital Order in LaMnO$_3$, Phys. Rev. Lett. **104**, 086402 (2010).

[15] Z. Popović and S. Satpathy, Origin of Charge-Orbital Order in the Half-Doped Manganites, Phys. Rev. Lett. **88**, 197201 (2002).

[16] A. J. Millis, P. B. Littlewood, and B. I. Shraiman, Double Exchange Alone Does Not Explain the Resistivity of La$_{1-x}$Sr$_x$MnO$_3$, Phys. Rev. Lett. **74**, 5144 (1995).

[17] A. J. Millis, B. I. Shraiman, and R. Mueller, Dynamic Jahn-Teller Effect and Colossal Magnetoresistance in La$_{1-x}$Sr$_x$MnO$_3$, Phys. Rev. Lett. **77**, 175 (1996).

[18] Ch. Jooss, L. Wu, T. Beetz, R. Klie, M. Beleggia, M. Schofield, S. Schramm, J. Hoffmann, and Y. Zhu, Polaron melting and ordering as key mechanisms for colossal resistance effects in manganites, Proc. Natl. Acad. Sci. USA **104**, 13597 (2007).

[19] K. Hirakawa and Y. Kurogi, One-dimensional antiferromagnetic properties of KCuF$_3$, Prog. Theor. Phys. Supp. **46**, 147 (1970).

[20] A. I. Liechtenstein, V. I. Anisimov, and J. Zaanen, Density-functional theory and strong interactions: Orbital ordering in Mott-Hubbard insulators, Phys. Rev. B **52**, R5467 (1995).

[21] J. E. Medvedeva, M. A. Korotin, V. I. Anisimov, and A. J. Freeman, Orbital ordering in paramagnetic LaMnO$_3$ and KCuF$_3$, Phys. Rev. B **65**, 172413 (2002).

[22] M. D. Towler, R. Dovesi, and V. R. Saunders, Magnetic interactions and the cooperative Jahn-Teller effect in KCuF$_3$, Phys. Rev. B **52**, 10150 (1995).

[23] E. Pavarini, E. Koch, and A. I. Lichtenstein, Mechanism for Orbital Ordering in KCuF$_3$, Phys. Rev. Lett. **101**, 266405 (2008).

[24] I. Moreira and R. Dovesi, Periodic approach to the electronic structure and magnetic coupling in KCuF$_3$, K$_2$CuF$_3$, and Sr$_2$CuO$_2$Cl$_2$ low-dimensional magnetic systems, Int. J. Quantum Chem. **99**, 805 (2004).

[25] I. Leonov, N. Binggeli, Dm. Korotin, V. I. Anisimov, N. Stojić, and D. Vollhardt, Structural Relaxation Due to Electronic Correlations in the Paramagnetic Insulator KCuF$_3$, Phys. Rev. Lett. **101**, 096405 (2008).

[26] J. Tong, C. Lee, M.-H. Whangbo, R. K. Kremer, A. Simon, and J. Köhler, Cooperative Jahn-Teller distortion leading to the spin-1/2 uniform antiferromagnetic chains in triclinic perovskites AgCuF$_3$ and NaCuF$_3$, Solid State Sci. **12**, 680 (2010).

[27] D. Kurzydłowski and W. Grochala, Large exchange anisotropy in quasi-one-dimensional spin-$\frac{1}{2}$ fluoride antiferromagnets with a $d(z^2)^1$ ground state, Phys. Rev. B **96**, 155140 (2017).

[28] S. Margadonna and G. Karotsis, Cooperative Jahn-Teller distortion, phase transitions, and weak ferromagnetism in the KCrF$_3$ perovskite, J. Am. Chem. Soc. **128**, 16436 (2006).

[29] S. Margadonna and G. Karotsis, High temperature orbital order melting in KCrF$_3$ perovskite, J. Mater. Chem. **17**, 2013 (2007).

[30] Y. Xiao, Y. Su, H.-F. Li, C. M. N. Kumar, R. Mittal, J. Persson, A. Senyshyn, K. Gross, and Th. Brueckel, Neutron diffraction investigation of the crystal and magnetic structures in KCrF$_3$ perovskite, Phys. Rev. B **82**, 094437 (2010).

[31] G. Giovannetti, S. Margadonna, and J. van den Brink, KCrF$_3$: Electronic structure and magnetic and orbital ordering from first principles, Phys. Rev. B **77**, 075113 (2008).

[32] Y. Xu, X. Hao, M. Lv, Z. Wu, D. Zhou, and J. Meng, Magnetic structure and orbital ordering in tetragonal and monoclinic KCrF$_3$ from first-principles calculations, J. Chem. Phys. **128**, 164721 (2008).

[33] G. Wang, Z. Li, L. Zheng, and Z. Yang, First-principles study on the orbital ordering of KCrF$_3$, Phys. Rev. B **84**, 045111 (2011).

[34] C. Autieri, E. Koch, and E. Pavarini, Mechanism of structural phase transitions in KCrF$_3$, Phys. Rev. B **89**, 155109 (2014).

[35] X. Ming, L. Xiong, H. Xu, F. Du, C. Wang, and G. Chen, First-principles study of orbital ordering in cubic fluoride KCrF$_3$, Chin. Phys. B **23**, 037401 (2014).

[36] F. L. M. Bernal, J. Sottmann, D. S. Wragg, H. Fjellvåg, Ø. S. Fjellvåg, C. Drathen, W. A. Sławiński, and O. M. Løvvik, Structural and magnetic characterization of the elusive Jahn-Teller active NaCrF$_3$, Phys. Rev. Mater. **4**, 054412 (2020).

[37] P. Blaha, K. Schwarz, G. Madsen, D. Kvasnicka, and J. Luitz, WIEN2K, An augmented plane wave + local orbitals program for calculating crystal properties (K. Schwarz, TU Wien, Austria, 2001).

[38] S. H. Vosko, L. Wilk, and M. Nusair, Accurate spin-dependent electron liquid correlation energies for local spin density calculations: A critical analysis, Can. J. Phys. **58**, 1200 (1980).

[39] V. Anisimov, F. Aryasetiawan, and A. Lichtenstein, First-principles calculations of the electronic structure and spectra of strongly correlated systems: The LDA +U method, J. Condens. Matter Phys. **9**, 767 (1997).

[40] P. R. Baral, N. Ahmed, J. Kumar, S. Nair, and R. Nath, Synthesis and physical properties of spin-1 honeycomb lattice Pb$_6$Ni$_9$(TeO$_6$)$_5$, J. Alloys Compd. **711**, 568 (2017).

[41] J. S. Smart, *Effective Field Theories of Magnetism* (Saunders, Philadelphia, 1966).

[42] J. B. Goodenough, *Magnetism and the Chemical Bond* (Interscience, New York, 1963).

[43] J. Kanamori, Superexchange interaction and symmetry properties of electron orbitals, J. Phys. Chem. Solids **10**, 87 (1959).

[44] P. W. Anderson, Theory of magnetic exchange interactions: Exchange in insulators and semiconductors, in *Solid State Physics* (Academic Press, New York, 1963), Vol. 14, pp. 99–214.

[45] K. I. Kugel and D. I. Khomskii, Crystal structure and magnetic properties of substances with orbital degeneracy, Zh. Eksp. Teor. Fiz. **64**, 1429 (1973).